Constraining Superbubble Dynamics with HST Imaging

Ishan Deb,[1,2] Crystal Martin,[3] and Zixuan Peng[3]
[1] *REU Program, University of California, Santa Barbara*
[2] *Haverford College*
[3] *Department of Physics, University of California, Santa Barbara*
(Dated: September 24, 2025)

Stellar feedback, the injection of energy and momentum from stars into the surrounding medium, plays a central role in galaxy evolution. Two key manifestations of stellar feedback are superbubbles and superwinds. Superbubbles are cavities of hot gas inflated by clustered supernovae, which can break out of the galactic disk. When this happens, hot gas is accelerated out of the galactic medium, called superwinds. While these phenomena are physically distinct, observational studies usually attribute the broad emission line components to galactic winds, but in a recent study in Peng et. al 2025, they show that the broad component could originate from superbubbles. This could mean that outflow properties, such as mass, momentum, and energy outflow rates, are overestimated, if the broad emission actually arises from superbubble shells.

Spectra alone are ambiguous: broad components may arise either from superwinds or from expanding superbubbles. High-resolution HST imaging provides a direct way to determine whether a shell is present. Once a shell is identified, I can test whether its physical properties (radius, velocity, luminosity) are sufficient to explain the observed spectral broadening. Using Hubble Space Telescope imaging of dwarf galaxies, I isolate emission line features through image alignment, and continuum subtracting. From these images, superbubbles are identified and their radii measured. The ages of the star clusters are determined through the Hydrogen Alpha ($H\alpha$) equivalent width, and ambient density measurements are performed from the flux of the emission line images. The surface brightness is plotted versus radius, and used to measure the half-light radius of the superbubbles. These parameters are used to calculate the expansion velocity and mechanical luminosity of the superbubbles via established theoretical models.

Preliminary results indicate that imaging-derived superbubble velocities agree with spectroscopic measurements in several systems. The morphologies and radius–velocity trends favor non-uniform (power-law) density profiles with one-sided, channel-like expansion; in such stratified media ($\kappa_\rho > 0$), the mechanical luminosity required to drive the observed bubbles decreases with increasing density gradient, so the energy needed to power the superbubble is lower than predicted by uniform-density models. Future work will expand the sample and directly compare imaging-based mechanical luminosities with spectroscopic estimates.

INTRODUCTION

Stellar feedback is a key driver of galaxy evolution, regulating star formation, redistributing gas and metals, and shaping the interstellar and circumgalactic media. Massive stars inject energy and momentum into their surroundings through stellar winds and supernovae, creating expanding bubbles of hot, low-density gas. When clustered together, these processes can collectively drive large-scale outflows and superbubbles that profoundly influence the galactic ecosystem. In particular, such feedback can evacuate channels through which ionizing radiation may escape, contributing to the ionization of the interstellar and intergalactic medium. While the escape of Lyman-continuum (LyC) photons has often been studied in the context of cosmic reionization, understanding the local processes that enable LyC escape also offers insight into how feedback operates in low-redshift, low-metallicity galaxies—more accessible analogs to early-universe systems.

A key manifestation of this feedback is the formation of superbubbles - large, expanding cavities of hot, low-density gas produced by many supernovae from star clusters. These can grow up to a kiloparsec scale in size and can expand out of the galactic disk entirely, causing what is called a blowout. When the hot gas reaches the cold circumgalactic medium, the hot gas accelerates out into the interstellar medium, causing galactic winds. These galactic winds bring metals, momentum, and energy out of the galaxy, regulating star formation and potentially opening density-bounded regions for LyC photons to escape. Superbubbles and superwinds therefore provide a crucial link between stellar feedback and the global ionization state of the universe.

Observationally, detecting and characterizing superbubbles presents a challenge. Historically, superbubbles and superwinds have often been grouped together in observational studies, with both treated as manifestations of large-scale outflows and modeled using similar broad spectroscopic components. As a result, distinctions between the two types of feedback have not been systematically explored in most datasets. However, recently in Peng et al. (2025)[1], they spectroscopically studied and modeled a difference in the kinematic outflows of superbubbles and superwind, in broad and very broad emission line components. He fitted the broad component of his

spectra, with a full-width half maximum (FWHM) value of 260 km/s, to superbubble emissions and the very broad component, with FWHM of 1000 km/s, to the emission from superwinds. Their distinction between superbubbles and superwinds is an important discovery and will help in research towards LyC escape and cosmic reionization, but his findings were made through spectroscopic data. In order to fully solidify the difference between superbubbles and superwinds, this must also be proven through optical analysis.

While in Peng et al., they used spectroscopic data from the Keck Cosmic Web Imager to study the velocity components of the ionized gas, our project aims to morphologically identify and characterize superbubbles using high-resolution imaging data from the Hubble Space Telescope (HST). In our project, I created continuum-subtracted hydrogen-alpha (Hα) images, which allowed us to identify bubble-like structures around star clusters in the galaxies, allowing me to estimate the physical radii of the superbubbles. From this, I can infer expansion ages through Spectral Energy Distribution (SED) fitting through Bagpipes, and calculate the expansion velocity and mechanical luminosity using models from Weaver et al. (1977) and Martin et al. (2024). The image-based approach provides a test hypothesis motivated by his analysis through optical and kinematic tools, proving or disproving the distinctions made between superbubbles and superwinds.

The evolution of superbubbles were modeled in Weaver et al. (1977)[2], where supernovae from a clustered stellar population inflate a bubble whose radius scales with time and mechanical luminosity. Weaver models the expansion velocity of the bubble in terms of size and age, providing a framework to interpret observed superbubbles in terms of their energy sources. Recent work by Martin et al. (2024)[3] applied this model to the spatially resolved KCWI spectroscopy of a low-metallicity, dwarf galaxy, finding that the size and kinematics of ionized gas bubbles were consistent with mechanical feedback from young star clusters. In Martin et al., they described a model that compares mechanical luminosity, radius, and velocity of the superbubble. Similar recent work by Geen and de Koter. (2021)[4] establishes a theoretical power law density model that takes the opening angle of the superbubble into account. These models provide a critical theoretical basis for interpreting the outflows of the observed superbubbles, especially when tied to the known ages and energetics of the star forming regions that power them.

METHODS

Emission Line Image Construction

To constrain key physical parameters from imaging, I first needed to generate continuum-subtracted Hα emission-line images. This required subtracting two HST images taken in different filters: an ON-band image, which includes the Hα emission line, and an OFF-band image, which captures only the stellar continuum. The continuum refers to the broadband stellar light that contributes to the total signal in the narrowband image but is not associated with the specific emission line of interest.

I attempted to performed this analysis on 2–3 HST images per galaxy for seven targets: J0934+5514, J0944-0038, J1016+3754, J1226+4829, J1418+2102, J1044+0353, and J0337-0502. These filters spanned wavelengths between 600–700 nm, ensuring that at least one filter contained the redshifted Hα emission line. J1044 and J0337 were added to the analysis later in the program. For J1044+0353, the OFF-band image was a narrowband filter capturing light centered around 462 nm.

Throughput Analysis and Filter Selection

To determine which filters to use for ON- and OFF-band images, I constructed throughput curves using data from the HST website for each filter available per galaxy. These curves show the relative transmission efficiency as a function of wavelength.

I computed the observed wavelength of Hα for each galaxy using:

$$\lambda_{\rm obs} = \lambda_{\rm rest} \times (1 + z) \tag{1}$$

where $\lambda_{\rm rest} = 6564.6\,\text{Å}$ is the vacuum wavelength of Hα, and z is the redshift. I overplotted this value as a vertical line on each throughput graph to identify which filter best captured the Hα line (ON-band) and which was offset (OFF-band). An example for J1418 is shown in Figure 1.

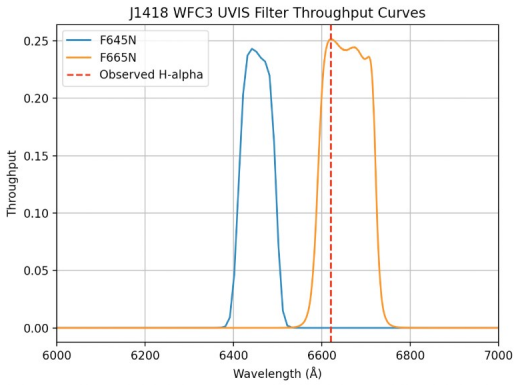

FIG. 1: Throughput graph of J1418. The two filters given were F665N and F645N. The observed Hα emission line is plotted vertically in dotted red. The graph shows F665N will be the ON-band image and F645N will be the OFF-band image.

Image Alignment

With ON- and OFF-band filters selected, I aligned the images to enable accurate subtraction. Initial misalignments varied, so I used code supplied to me to apply a geometric transformation based on common point sources—foreground stars appearing in both filters.

To identify these stars, I used *SAOImage DS9* and cross-referenced the fields with Sloan Digital Sky Survey (SDSS) images provided by my mentor. These reference points were used to compute a translational matrix via affine transformation. While standard affine transformations require three matched sources to solve for the center of the clusters to match the images, most of my images had one or two suitable stars. I therefore implemented a simplified transformation that reduced the minimum required matching background stars to one.

This approach successfully aligned ON to OFF images for all galaxies except J1226 and J0337. J1226 lacked usable point sources and had corrupted data in its ON-band image near the central cluster. As a result, J1226 was excluded from further analysis, and will be addressed in future work to be added to the sample. For J0337, the only OFF-band images available were wideband filters, which led to incorrect continuum subtraction. Some analysis of J0337 is done using only the ON-band image, like the velocity due to finding the superbubbles in the ON-band image, but full analysis is not possible without a continuum subtracted image. Future work will hopefully include this in the sample as well.

Continuum Subtraction and Scaling

Once aligned, I performed the subtraction using:

$$\text{DIFF} = \text{ON} - (\text{scaling factor}) \times \text{OFF} \tag{2}$$

Initially, I used a scaling factor of 1 to test the output. However, this resulted in under-subtracted images, as the scaling factor must account for both filter transmission differences and the slope of the galaxy's stellar continuum.

To determine the correct factor for each galaxy, I coded a loop that generated 15 subtracted images using scaling factors from 0.5 to 2.0. For each, I examined a known point source and computed the median pixel value and the histogram of a box centered on that source. The optimal scaling factor minimized the median to zero and eliminated skewed tails in the histogram, indicating proper subtraction. The scale values calculated for each are shown in table I.

TABLE I: Scaling factors used for each galaxy during continuum subtraction.

Galaxy	J0934	J0944	J1016	J1418	J1044
Scaling Factor	2.000	1.397	1.621	1.820	0.69

Signal-to-Noise Verification

After scaling, I examined whether subtraction preserved faint filamentary structures (possible superbubbles), particularly in J0934 and J1016. In some cases, low-surface-brightness features were lost—likely overwhelmed by noise introduced from the OFF-band image.

To quantify this, I generated signal-to-noise ratio (SNR) maps by calculating the extrinsic and intrinsic pixel-wise errors for each image, using formulas that were shown in a comprehensive guide to HST Drizzling written by Yuan Li. I was given this document as reference for the error analysis section. The extrinsic Poisson noise is the shot-noise arising from photon counting in each image (source + sky). The equation for each pixel is:

$$\sigma_{\text{ext}} = \sqrt{\frac{\texttt{drz}}{\texttt{EXP}}} \tag{3}$$

where `drz` is the pixel value in the drizzle-combined image and `EXP` is the corresponding exposure weight from the WHT map.

Intrinsic noise was measured using the standard deviation σ in a blank sky region of the image. The intrinsic noise captures non-Poisson fluctuations (e.g., read noise, flat-field residuals, background structure, drizzle resampling correlations). These were combined in quadrature to compute total errors for ON and OFF images.

The SNR of the difference image was then calculated using:

$$\sigma_{\text{diff}} = \sqrt{\sigma^2_{\text{on, tot}} + (\text{scaling factor} \times \sigma_{\text{off, tot}})^2} \tag{4}$$

and SNR was defined as the pixel value in the difference image divided by $\sigma_{\rm diff}$.

In regions of interest, star clusters showed SNR $>$ 1–2, but faint filaments typically had SNR between 0.5–1. Background regions fell between 0–0.75. These values confirmed that OFF-band noise was suppressing faint emission.

To address this, I implemented a thresholding technique: values in the OFF-band image below the 95th percentile of the difference SNR image distribution were set to zero, removing the high noise in the background of the OFF-band images. This thresholded OFF-band image was then rescaled and subtracted from the ON-band image. As a result, the filamentary structures were recovered in all galaxies, enabling reliable morphological analysis. Once completed, the emission line images were used to compute the variables needed to calculate expansion velocity and mechanical luminosity: superbubble radius, expansion time, ambient density, and opening angle.

Superbubble Identification

Once I obtained pure emission-line images for the four workable galaxies, I used the filamentary structures visible in these images to estimate superbubble radii. The OFF-band images located the central star clusters, and the emission-line images were used to draw elliptical regions in DS9 delineating each superbubble. Each galaxy and its corresponding superbubble(s) are shown in Figures 2–7.

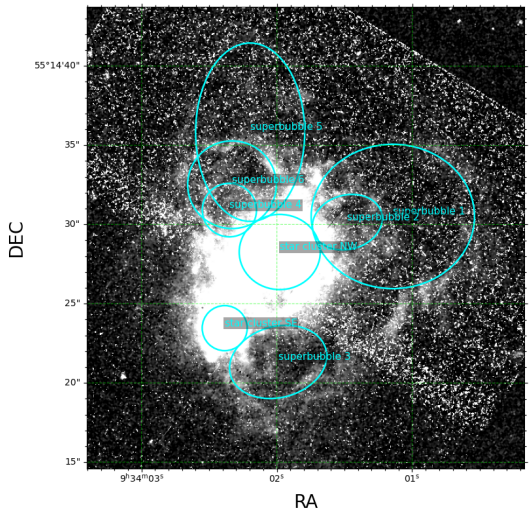

FIG. 2: Superbubbles in J0934. Up to seven candidates appear around the northeast and southwest clusters; overlapping structures may reflect projection. I adopt bubbles 1, 3, and 6 for velocity and luminosity analysis.

For J0934, I identified up to seven candidate superbubbles: two families of filaments extend from the northeast cluster, and one bubble is apparent near the southwest cluster. Many features overlap and may trace a single expanding structure projected onto the plane of the sky. For velocity and luminosity analysis, I used superbubbles 1, 3, and 6 due to the fact they cover all three regions where I see superbubbles and are easily distinguishable.

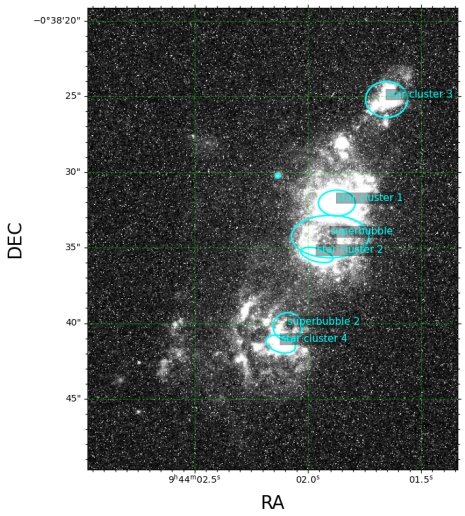

FIG. 3: Superbubbles in J0944. Two bubbles are detected; the southern pair of clusters appears to power a feature extending northward.

In J0944, two distinct superbubbles are present. This galaxy hosts four major clusters, with the two southern clusters driving a bubble extending northward.

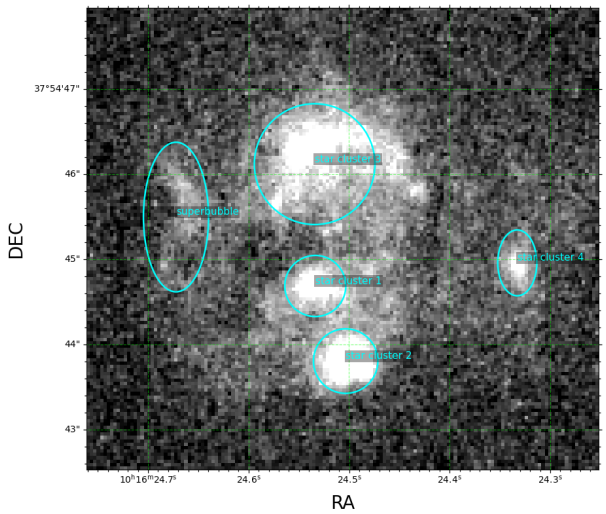

FIG. 4: Superbubble in J1016. A single, more irregular candidate is detected; its absence in the OFF-band and presence in the subtraction supports an Hα origin.

For J1016, one ambiguous bubble was identified. It is less circular and less clearly connected to its powering cluster than in other systems, but the feature is absent in

the OFF-band and present in the subtraction, consistent with line emission. I interpret it as a bubble likely blown from the northernmost cluster.

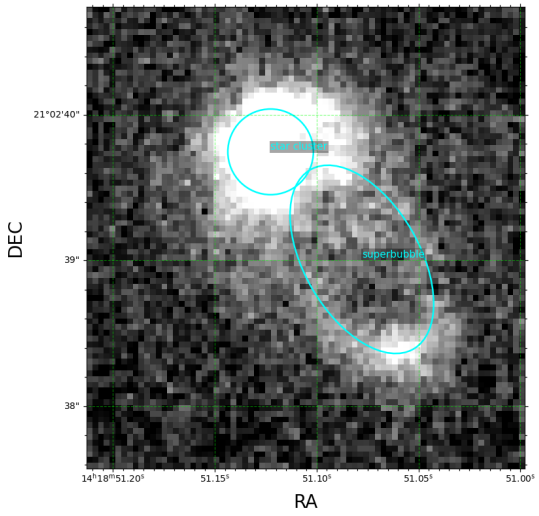

FIG. 5: Superbubble in J1418. A single, high-contrast bubble extends southwest from the central cluster.

For J1418, one well-defined bubble is seen, extending to the southwest from a single prominent cluster.

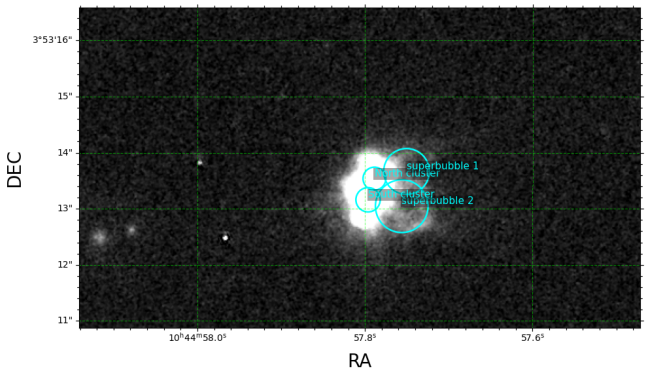

FIG. 6: Superbubble in J1044. A single, high-contrast bubble extends southwest from the central cluster.

For J1044, two superbubbles are seen expanding, one to the northwest, and one to the southwest.

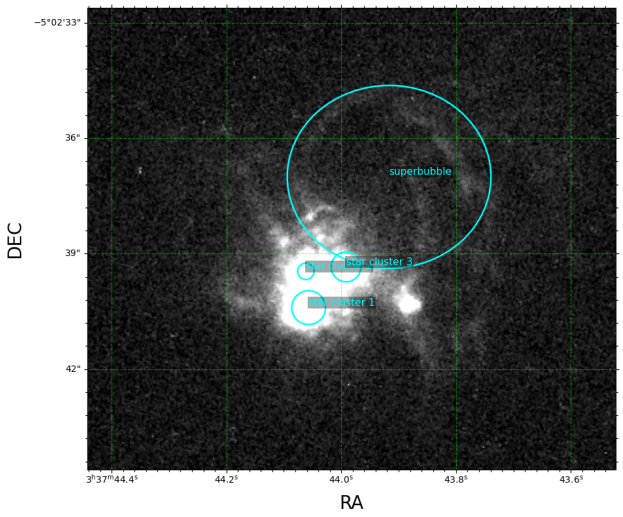

FIG. 7: Superbubble in J0337. A single, high-contrast bubble extends southwest from the central cluster.

For J0337, a large superbubble can be seen in the north region, extending from the northern most star cluster.

To measure radii, I used the DS9 ellipse region parameters. Because many bubbles expand preferentially in one direction, I use the measured diameter as an effective radius for comparison with spherical models (a conservative choice for one-sided structures). Pixel radii were converted to arcseconds using the image WCS/pixel scale from the FITS headers, and then to parsecs using the galaxies' redshifts and a standard cosmology via an online calculator.

Expansion Time and Age Estimates

In order to estimate expansion velocities, I require an expansion time. Superbubbles are powered by clustered supernovae; for young systems a supernova onset of $\sim$ 3 Myr is reasonable. For a cluster age $t_\star$, I therefore adopt $t_{\rm exp} = t_\star - 3$ Myr.

As a preliminary step, I surveyed the literature for cluster ages in our sample. Ages were available for J0934 (both the northwest and southeast clusters), J0944 (the second-brightest cluster, ordered from top to bottom), and J1418 (the cluster associated with the superbubble). The clusters coincident with the superbubbles in J0944 and J1016 lacked published ages for the specific powering clusters. For J1044, for expansion time and density, literature measurements from Martin et al. (2024)[3] were used.

Then I adopted the method of using equivalent width of the Hα to estimate the star cluster ages using Starburst99. This is possible due to the fact that the strength of the Hα emission is directly correlated to the age of the star clusters. The equivalent width of Hα is a measure of a spectral line's strength relative to the adjacent

stellar continuum. Young star clusters produce many energetic photons, capable of ionizing neutral hydrogen atoms. When ionized, the hydrogen atom loses its electron, allowing a free electron to then recombine with an already ionized hydrogen atom. When this atom recombines with the electron, it emits a photon. The strength of the photon is determined by the energy level drop of the hydrogen atom, with the Hα emission line being the change from a n=3 to n=2 state. As star clusters age, they emit less energizing photons, allowing a direct correlation between the equivalent width and age. A model called Starburst99 takes different parameters into account, including metallicity, which I knew for each galaxy, and creates many different model plots, including Hα equivalent width vs. age. I adopted metallicities consistent with each galaxy: $Z = 0.0004$ for J0934, $Z = 0.001$ for J1016, and $Z = 0.002$ for J0944 and J1418. The observed equivalent width was computed from the continuum-subtracted (difference) image and the OFF-band continuum image as

$$\mathrm{EW}_{\mathrm{obs}} = \frac{F_{\mathrm{diff}} - F_{\mathrm{off}}}{F_{\mathrm{off}}} \times W_{\mathrm{nb}}, \tag{5}$$

where W_{nb} is the effective rectangular width of the narrowband filter. The rest-frame equivalent width was obtained by dividing by $(1 + z)$. For each cluster, I overplotted the measured rest EW as a vertical line on the model EW–age curves and read off the corresponding age from the intersection, shown in Figure 13. An example for J1418 can be seen in Figure 8.

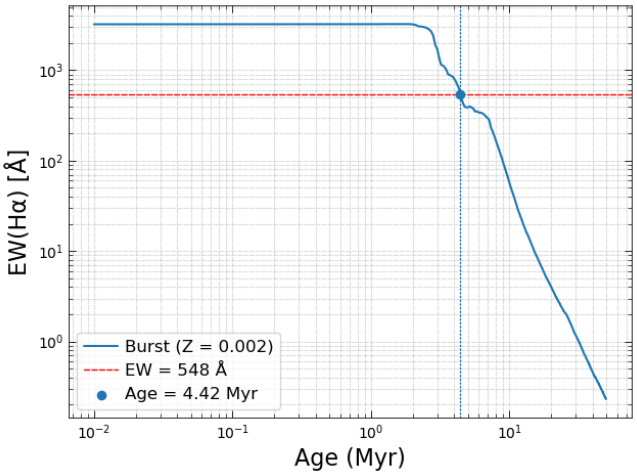

FIG. 8: Equivalent Width vs. Age plots for star cluster in J1418. Age is 4.42 Myr old.

The EW-based ages agree with literature values for J0944 and J1418 within uncertainties. For J0934, the EW-derived ages differ from the published values; this method is comparatively imprecise and can yield large uncertainties, especially where the EW–age curve is shallow, which in turn inflates the velocity and mechanical-luminosity uncertainties.

Ambient Density of the ISM

Another variable to constrain was the ambient density of the interstellar medium (ISM) around the superbubble. To calculate the ambient density, both the flux of the powering star cluster and the associated superbubble were required. Using the image headers of the HST FITS files, I converted the raw counts in the emission-line images to flux units. Specifically, I multiplied the counts (in counts s^{-1}) by `PHOTFLAM`, the inverse sensitivity, to obtain flux densities in units of erg s^{-1} cm^{-2} Å^{-1}. Multiplying by `PHOTBW`, the effective filter bandwidth, removed the wavelength units and produced emission-line fluxes in units of erg s^{-1} cm^{-2}.

Apertures were then defined around each star cluster and its associated superbubble. The apertures were modeled as *conical regions* extending from the center of the star cluster to the end of the superbubble. A conical geometry was chosen because the imaging showed that the superbubbles were not spherically expanding but rather extended preferentially in one direction. This approach accounts for three-dimensional structure using two-dimensional images, with the cone apex placed at the cluster center and the base radius spanning the observed superbubble. For each region, I measured the flux, radius, and height of the cone.

The galaxy distances were calculated from their redshifts and converted into megaparsecs (Mpc). With these distances, the Hα luminosity of each region was determined using Equation 6:

$$L_{H\alpha} = 4\pi D^2 F_{H\alpha}, \tag{6}$$

where D is the distance in cm and $F_{H\alpha}$ is the observed flux. This yields the intrinsic energy emitted in the Hα line per second.

Each Hα photon has an energy given by

$$E_{H\alpha} = h\nu_{H\alpha} = \frac{hc}{\lambda_{H\alpha}}, \tag{7}$$

where h is Planck's constant, c is the speed of light, and $\lambda_{H\alpha}$ is the rest wavelength of Hα in vacuum. The corresponding rate of Hα photon emission is therefore

$$N_{H\alpha} = \frac{L_{H\alpha}}{E_{H\alpha}}. \tag{8}$$

Because not every recombination event produces an Hα photon, I used the case B effective recombination coefficient, $\alpha_{\mathrm{eff},H\alpha}$, evaluated at two representative temperatures, $T = 10{,}000$ K and $T = 20{,}000$ K (values from Osterbrock (1989)[5]). Since the actual gas temperatures

are unknown, I adopted the mean of the two density estimates and propagated the difference as a systematic uncertainty. The emission measure (EM) was then calculated using Equation 9:

$$\mathrm{EM} = \frac{L_{H\alpha}}{h\nu_{H\alpha}\,\alpha_{\mathrm{eff},H\alpha}}. \tag{9}$$

To estimate the ionized volume, each superbubble was modeled as a cone,

$$V = \tfrac{1}{3}\,\pi R^2 h,$$

where R is the base radius and h is the height. Both R and h were measured in pixels, converted to arcseconds, then to radians, and finally to physical lengths in cm. Combining the emission measure with the volume, the root-mean-square (rms) electron density was obtained from Equation 10:

$$n_{e,\mathrm{rms}} = \sqrt{\frac{6}{5}\,\frac{\mathrm{EM}}{V}}. \tag{10}$$

The prefactor $\sqrt{6/5}$ is a helium correction that converts from $n_e n_p$ to n_e^2, following Equation 9 of Martin et al. (2024)[3]. This procedure yields the rms electron density for each superbubble region.

Constraining the Opening Angle

Another parameter required for the luminosity calculation was the opening angle of the outflow. In first-order approximation, the opening angle was parametrized as 4π, corresponding to a spherical outflow. However, once the first-order analysis indicated that a power-law approximation was more appropriate, it became necessary to constrain the opening angle directly from the imaging geometry.

The opening angle was constrained using the continuum-subtracted emission-line images, where I measured the position angles (PAs) of the two edges of the superbubble cavity relative to the powering star cluster. These were obtained using the line region profile in DS9, which returns the PAs in degrees. The difference between the two position angles defines the full opening angle of the superbubble, denoted as ϕ:

$$\phi = |\mathrm{PA}_1 - \mathrm{PA}_2| \tag{11}$$

The half opening angle is then

$$\theta = \tfrac{1}{2}\phi. \tag{12}$$

To translate this geometry into the solid angle subtended by the outflow, I used the spherical-cap formula to constrain the opening angle, shown in Equation 13:

$$\Omega = 2\pi(1 - \cos\theta), \tag{13}$$

where Ω is the solid angle in steradians. If the outflow were a bicone, this value would be doubled, but here I restricted the measurement to a single cone. The uncertainty of this measurement was determined from the variability of the PAs, which propagates into variance in ϕ. With the opening angle constrained, all variables required for the velocity and luminosity calculations are now in place.

Constraining the Half-Light Radius

To solve for the mechanical luminosity, it was necessary to constrain the half-light radius of the powering star clusters. The half-light radius (r_{50}) was measured from the stellar continuum traced in the OFF-band images, ensuring that the measurements reflected the underlying stellar populations rather than nebular emission.

The calculation was performed using a custom Python script built on `astropy` and `photutils`. The procedure was as follows:

1. The OFF-band images were opened as `FITS` files and cropped to focus on the region surrounding each target cluster.

2. Source segmentation was performed using the `photutils.segmentation` module. This step identifies sources in the image above a chosen detection threshold and creates masks to isolate individual clusters.

3. When clusters were blended or in close proximity, the segmentation map was refined using deblending algorithms to ensure that each cluster's light was measured independently.

4. With the segmentation map defining the cluster boundaries, concentric circular annuli centered on the cluster were constructed. The flux within each annulus was summed to build a cumulative growth curve of flux versus radius.

5. The total flux was taken as the asymptotic value of the growth curve, and the half-light radius r_{50} was identified as the radius enclosing half of this flux.

An example of this procedure is shown in Figure 9, where the vertical dashed line marks the radius at which the cumulative flux reaches half the total light of the northwest cluster in J0934.

For J0337, suitable OFF-band images were not available, preventing measurement of r_{50} and leaving the derived mechanical luminosities unconstrained. Once OFF-band data are obtained for this system, the same procedure can be applied to obtain the cluster radii.

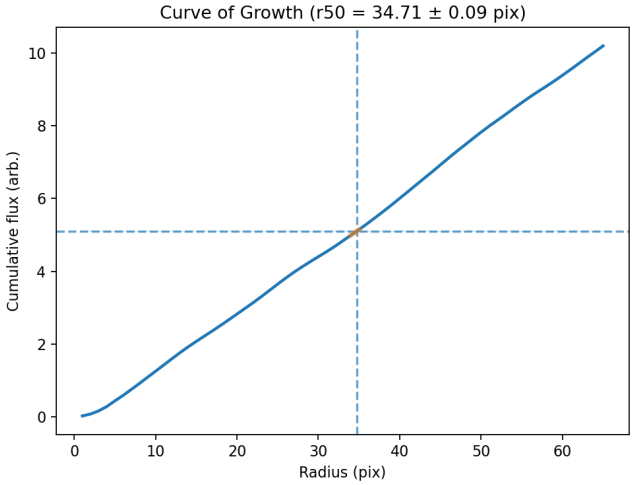

FIG. 9: Half-light radius measurement for the northwest cluster in J0934. The image was cropped to the region of interest and sources were segmented to isolate the target cluster. The vertical dashed line marks the radius enclosing half of the total light.

For the remaining galaxies, this segmentation-based method was applied to all clusters associated with superbubbles, yielding r_{50} values that are compiled in Figure 16.

RESULTS

To interpret the morphology and energetics of superbubbles observed in our HST emission-line images, I first compare spectroscopic measurements with predictions from the classical wind-blown bubble model of Weaver et al. (1977)[2]. This model describes the expansion of a bubble into a uniform interstellar medium and provides analytic relations for bubble radius, expansion velocity, and mechanical luminosity. I then calculated the expansion velocity and mechanical luminosity of each bubble using a power law model, and once again compare that to the spectroscopic data.

Models

In the Weaver framework, continuous energy injection from stellar winds drives a layered superbubble structure consisting of an inner free-streaming wind, a termination shock at radius R_1, a region of shocked wind bounded by a contact discontinuity at R_C, and an outer shell of swept-up interstellar medium at R_2. This pressure-driven configuration forms the basis for deriving the observable properties of superbubbles. In particular, the expansion velocity V is related to the bubble radius R

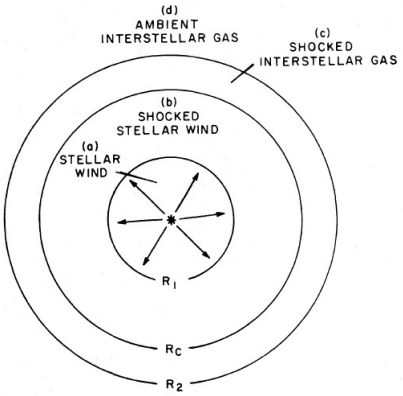

FIG. 10: Schematic of the Weaver model superbubble showing the structure of the wind-blown bubble, including the shocked wind and swept-up ISM shell. Adapted from Weaver et al. (1977)[2].

and age t by

$$V = \frac{3}{5} \times \frac{R}{t}, \tag{14}$$

which assumes uniform ambient density. The corresponding mechanical luminosity can be estimated following Martin et al. (2024)[3]:

$$L_w = 1.85{\times}10^{41} \left(\frac{R}{340\ \mathrm{pc}}\right)^2 \left(\frac{V}{100\ \mathrm{km/s}}\right)^3 \left(\frac{n}{4\ \mathrm{cm}^{-3}}\right) \left(\frac{\Omega}{4\pi}\right), \tag{15}$$

For our initial estimates I set $\Omega = 4\pi$, corresponding to spherical expansion.

While these first-order calculations are useful for verifying our measurement procedure, they assume a uniform ISM and therefore cannot fully capture the environments of real galaxies. When compared to spectroscopic velocities from Peng et al. (2025)[1], I found that Weaver-model predictions systematically deviated from the observed values. The expansion velocities calculated using the Weaver model were 150 km/s off the spectroscopic estimates. This motivated us to adopt generalized models that account for radial variations in ambient density.

Following Martin (1996)[6], I considered power-law density profiles of the form $\rho \propto r^{-\kappa_\rho}$, which modify the bubble expansion law to

$$V = \eta \times \frac{R}{t}, \tag{16}$$

where η depends on the density gradient κ_ρ. Steeper gradients ($\kappa_\rho > 0$) reduce η, lowering the inferred velocity for a given radius and age. I tested values of κ_ρ from 0 (uniform density) to 3 to evaluate which best matched the observed bubble kinematics.

I further refined the energetics using the mechanical luminosity formulation of Martin (1996), which incorporates power-law density gradients. In this formalism, the

input mechanical luminosity relative to the average density is expressed as

$$\frac{L_{in}(1)}{\bar{\rho}(1)} = \frac{\eta_{in}}{\xi\Gamma\eta^3} R_s(1)^{\frac{5\eta-3}{\eta}} v^3 R_s^{\frac{3(1-\eta)}{\eta}}, \tag{17}$$

where ξ and Γ are constants of order unity in Ostriker and McKee (1988) [7]. For our analysis, I assume $L_{in}(1) = L_w$. Because the observed bubbles are not spherical, I also included the measured opening angle in the luminosity calculation. This equation was found through the paper in Geen and De Koter (2021) [4], in which they give the theoretical equation for radius using mechancial luminosity and opening angle. The equation given for radius in this paper is:

$$r_\omega(\omega, t) = (A_\omega(\omega, \Omega) L_\omega \rho_0^{-1} r_0^{-\omega} t^3)^{1/(5-\omega)} \tag{18}$$

Where

$$A_\omega(\omega, \Omega) = \frac{4\pi}{\Omega} \frac{1-\omega/3)(1-\omega/5)^3}{(1-2\omega/7)(1-\omega/11)} \frac{250}{308\pi} \tag{19}$$

Where r_0 is injection radius, which we substituted for the half-light radius of the star cluster and superbubble due to the fact we cannot constrain the injection radius, and the half-light radius, r_{50} of the star clusters powering the superbubbles is a good estimate for this. ω is the density gradient, so $\omega = \kappa_\rho$. Rearranging these equations and inserting velocity allows for a final equation for the mechanical luminosity that includes the half-light radius and the opening angle.

$$L_w = \frac{\Omega}{4\pi} \rho_0 r_{50}^{\kappa_\rho} R_s^{2-\kappa_\rho} v^3 C(\kappa_\rho) \tag{20}$$

where $C(\kappa_\rho)$ are constants defined as:

$$C(\kappa_\rho) = (\frac{5-\kappa_\rho}{3})^3 \frac{308\pi}{250} \frac{1-2\kappa_\rho/7)(1-\kappa_\rho/11)}{(1-\kappa_\rho/3)(1-\kappa_\rho/5)^3} \tag{21}$$

This framework allows us to transition from simple Weaver-model predictions to more realistic power-law models, directly constrained by our imaging-based measurements of radius, velocity, density, opening angle, and half-light radius. In the following sections, I compare these model-based estimates of expansion velocities and mechanical luminosities to spectroscopic results, testing whether superbubbles and superwinds can be distinguished using imaging alone. Usage of the power law model led to the following results. For the flow of the paper, J1418 has been chosen as the model galaxy to show the plots for in the following sections. The values discussed will be from the appendix with the full table of values and all plots.

Table of Values for each Superbubble at Different Density Gradients

Table II shows all used and measured values for each superbubble in the 5 total galaxies. Values for cluster age and ambient density were taken from Martin et al. (2024) [3] for J1044.

Radius vs Velocity plots

Figure 14 shows radius vs expansion velocity at different density gradient values for the distinct superbubbles found. The red dot is the spectroscopic velocity plotted with the radius found through optical analysis. Below is an example of the radius vs expansion velocity plot of J1418.

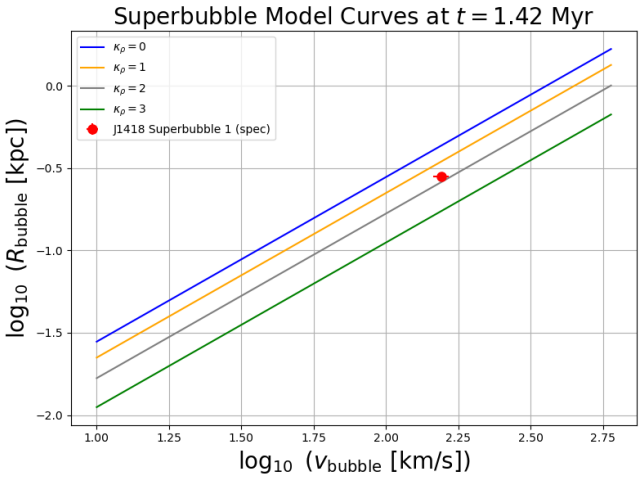

FIG. 11: J1418 Radius vs Expansion Velocity. I see the spectroscopic velocity lies near the $\kappa_\rho = 2$ line, showing the best fit density gradient for J1418 is $\kappa_\rho = 2$.

The superbubble model curves provide a useful framework for comparing theoretical expectations with the observed spectroscopic measurements of radius and velocity. For J0934 and J1016, however, the spectroscopic points do not align with the model predictions for any of the assumed density gradients. In J0934, this mismatch may be attributed to uncertainties in the stellar population age estimates: the equivalent width–age relation from Starburst99 yields ages that differ from those reported in the literature. Even when adopting literature ages, the observed spectroscopic velocities remain too high. This discrepancy could stem from insufficient spatial resolution in the spectra, which may capture more than just the expanding superbubble and thus artificially broaden the velocity signature. For J1016, the identification of the superbubble itself is uncertain. The emission feature chosen is the only structure visible in the continuum-subtracted image but absent in the OFF-band. However, its morphology is convex rather than concave, unlike typical superbubble outflows, suggesting it may not represent a true superbubble.

In contrast, the J0944 superbubbles show good agreement with the models, with both spectroscopic measure-

ments falling near the predicted relation for a density gradient of $\kappa_\rho = 3$. Similarly, the J1418 superbubble lies between the $\kappa_\rho = 1$ and $\kappa_\rho = 2$ models, but closer to $\kappa_\rho = 2$, again indicating a preference for non-uniform, higher-gradient density profiles. The J1044 superbubbles both lie very close to $\kappa_\rho = 2$ as well. Finally, J0337 shows a density gradient of $\kappa_\rho = 1$, showing a lower, but still not uniform, density gradient. Together, these comparisons suggest that superbubbles tend to evolve in environments with steep density gradients, rather than uniform media.

Values for J0337 were used from Mingozzi et al. (2025)[8] in order to see a radius vs. velocity plot of the superbubble found in this galaxy. Without a suitable OFF-band image, this is all the analysis that can be done.

This tendency toward higher density gradients naturally links to the mechanical luminosity results. As shown in the L_w–v diagrams (Figures 15a - 15e), the derived mechanical luminosities decreases with steeper density gradients, implying that superbubbles expanding into stratified environments require less energy input to reach their observed sizes and velocities. The following section explores this relationship in detail.

Mechanical Luminosity Calculations

Once I calculated the mechanical luminosity of all superbubbles at different κ_ρ values, I could plot the mechanical luminosity vs expansion velocity for each superbubbles at different density gradients. These are shown in Figure 15. Below is the plot of mechanical luminosity vs. expansion velocity for J1418.

The L_w–v relations show a systematic decrease in mechanical luminosity with steeper density gradients (κ_ρ). Physically, this indicates that outflows propagating in regions of higher density gradients require less energy injection to reach the observed radii and velocities. This makes sense physically since a power-law density profile implies that the gas density decreases with increasing radius, as the less dense the region the superbubble is pushing into, the less energy required to power the expansion.

Some error bars highlight substantial uncertainties in the derived L_w, dominated by uncertainties in ρ and the expansion velocity v. Since $L_w \propto v^3$, even modest uncertainties in the velocity propagate to large errors in the inferred luminosities. This effect is particularly evident in galaxies like J1044 and J0944, where the spread in v across superbubbles leads to significant vertical scatter in L_w.

Together, these results show that the assumption of a uniform ISM ($\kappa_\rho = 0$) overestimates the energy requirements of the superbubble expansion. The consistency of lower L_w at steeper density slopes supports a picture

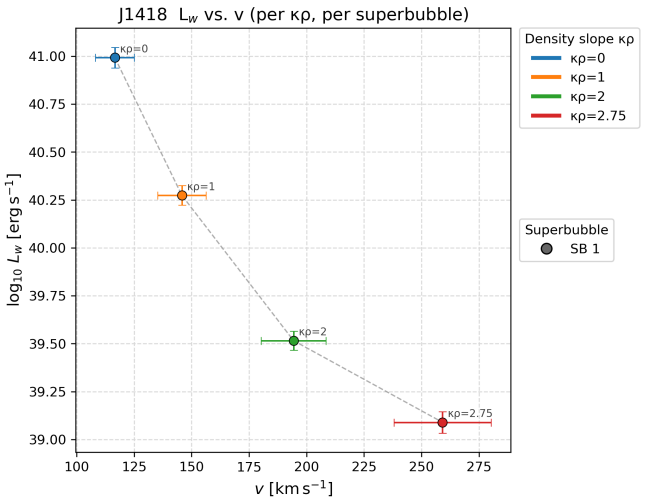

FIG. 12: Mechanical Luminosity vs. Expansion Velocity with uncertainties for J1418. There is a consistent decrease in mechanical energy required to power the superbubble per density power law. The fit seems to follow an exponential decay pattern.

where these outflows preferentially expand into stratified environments, rather than into homogeneous gas distributions, then causing the superbubble to spend less energy on expansion. This can also be seen in the images, where the bubbles expand in one direction. A hypothesis is that these are low-density regions and that the bubble wants to expand in the path of least resistance.

DISCUSSION

Our results are subject to several layers of uncertainty, each of which plays an important role in shaping the robustness of our conclusions. The largest source of error arises from the ages of the powering clusters. In J0934, the cluster ages derived from Hα equivalent width measurements do not agree with published literature values, highlighting the sensitivity of the equivalent width method to assumptions about stellar population models and metallicity. However, usage of either age values leads to a discrepancy between the calculated velocities for each density model and the spectroscopic velocity found in Peng et al. (2025)[1]. For J1016, no literature values exist, leaving the equivalent width calculation as the only available approach. This creates significant uncertainty, since small errors in equivalent width translate to large shifts in age estimates, particularly at young cluster ages where the EW–age relation is steep. Because expansion time is defined as $t_{\rm exp} = t_\star - 3$ Myr, these uncertainties propagate directly into the derived expansion velocities. As a result, cluster ages represent the dominant source of error in our analysis, limiting the precision with which expansion dynamics can be constrained.

A second important uncertainty arises in our estimates of the ambient density. To calculate density, I relied on assumptions about both geometry and physical conditions. I extracted fluxes using a conical aperture that encompassed the bubble, but this choice inevitably includes emission from the powering cluster itself. This contamination biases the luminosity upward, which in turn inflates the estimated ambient density. Furthermore, the recombination coefficient depends on gas temperature. I adopted values at 10^4 K and 2×10^4 K, then averaged the results, but this procedure introduces systematic error since real nebular temperatures may vary spatially and lie outside this narrow range. Although density affects the derived mechanical luminosity only weakly, these combined uncertainties complicate efforts to place absolute values on ρ. Thus, while our relative density comparisons between bubbles remain informative, absolute normalization is less secure.

A third challenge lies in the identification of superbubbles themselves. In systems such as J1016, the candidate structure lacks the characteristic concave shell morphology expected of a clear superbubble, raising the possibility that the observed feature may be an overlapping filament or irregular emission region rather than a coherent bubble. Misclassification of features in the imaging introduces another layer of uncertainty, as subsequent dynamical and energetic calculations rest on this initial identification.

Despite these uncertainties, meaningful physical insights emerge from the comparison between imaging-derived expansion velocities and spectroscopic values. For the radius vs. velocity plots of J0944, J1418, J1044, and J0337, the observed points align well with model curves corresponding to non-uniform density profiles, with κ_ρ values between 1 and 3. This range of density gradients suggests that superbubbles preferentially expand into directions of decreasing ambient density, which is consistent with the observed one-sided, elongated morphologies. In contrast, a uniform medium ($\kappa_\rho = 0$) would produce spherical, symmetric expansions, similar to the idealized Weaver model. The fact that our systems show stronger agreement with non-uniform profiles reinforces the idea that ISM structure, including density gradients and anisotropies, strongly regulates bubble growth and breakout. This provides further observational evidence that feedback does not couple isotropically to the ISM, but rather exploits paths of least resistance.

Finally, I turn to the energetics of the superbubbles. Peng et al. (2025) [1] estimates that core-collapse supernovae inject mechanical power at the level of $\sim 3\times10^{41}$ erg s^{-1} into the surrounding medium. Our derived mechanical luminosities for bubbles that agree with spectroscopic velocities lie in the range 10^{36}–10^{41} erg s^{-1}. These values are systematically lower than the input rate, which is physically expected: a major fraction of the injected energy goes into bubble expansion, with the remainder dissipated through radiative cooling, turbulence, and leakage of hot gas into low-density channels. Our results suggest that bubble expansion consumes the majority of the available energy, leaving only $\sim 10^1$–10^4 erg s^{-1} for radiative cooling under the assumptions of our model. The one notable exception is J0337, where the derived mechanical luminosity exceeds 3×10^{41} erg s^{-1}, although still within the error budget. This could reflect either an overestimate in cluster age or density, or enhanced energy coupling in this particular system. More generally, the overall agreement between expected input energy and observed mechanical luminosities lends support to the physical picture in which superbubble expansion dominates the energy budget of stellar feedback, while a lesser fraction goes to radiative cooling and other sources. I also see, in the luminosity vs velocity power law graphs, how the mechanical luminosity decreases with a high density gradient, further showing how the superbubble preferentially expand into zones of high density gradient, as they require less energy to expand and allow for higher bubble speeds that match the spectroscopic data.

Taken together, these results highlight the dual role of uncertainties and insights in this analysis. While cluster ages, density assumptions, and morphological identifications remain limiting factors, the overall consistency between imaging- and spectroscopy-based measurements supports the robustness of the conclusion that superbubbles expand preferentially along low-density channels, consuming most of the injected CCSN energy in the process. The findings in this paper show that uniform density models, like shown in Weaver et al. (1977) [2], underpredict the expansion velocity of superbubbles, thus overestimating the mechanical luminosity required to power the expansion of the superbubble. Power law density gradients are required to match realistic estimates of expansion velocity and mechanical luminosity. With most superbubbles showing values of $\kappa_\rho > 0$, the physical picture fits what I see in the Hubble Space Telescope images, one-sided, channel-like expansion into areas of decreasing ambient density, which shows that the bubbles may follow paths of least resistance rather than expanding spherically. For fixed radius and expansion time, the inferred mechanical luminosity L_w decreases with increasing κ_ρ, because a steeper, falling-density profile reduces the work the shell must do as it advances—naturally reproducing the observed radii–velocity pairs without invoking unrealistically large power.

FUTURE WORK

I will be continuing this project throughout the 2025–2026 academic year. A primary focus will be to constrain cluster ages more robustly using spectral energy distribution (SED) fitting, which should significantly re-

duce the current large uncertainties in expansion time. Getting better age estimates should help the measured values of velocity for J0934 and J1016 to match the spectroscopic velocity found in Peng et al. (2025)[1]. In addition, I aim to obtain spectroscopic measurements of mechanical luminosity in order to directly compare the imaging-derived values presented here with independent spectral estimates. In some cases, deeper or higher-resolution spectroscopy will be required, as the existing data for certain galaxies are not sufficiently sensitive, leading to over- or underestimates of spectral quantities such as velocity.

My work will also extend these analysis techniques to additional galaxies, thereby expanding the catalog of systems available for comparison with spectroscopy. A larger sample will provide stronger evidence for distinguishing between superbubbles and superwinds, and for identifying the outflow components associated with superbubbles. Fixing the corrupted frame in J1226 and getting a narrowband filter for J0337 will allow these two galaxies to be used for full analysis.

Future work may also connect with the studies of Katherine Kudla, who has examined low-density regions in similar low-metallicity dwarf galaxies using [O III]/[O II] line ratios. Her findings could complement this project by linking superbubble expansion to the lowest-density channels in the ISM, further supporting the hypothesis that superbubbles preferentially propagate along paths of least resistance.

ACKNOWLEDGMENTS

This work was supported by the National Science Foundation through REU grant PHY-2349677. I thank Dr. Crystal Martin, Zixuan Peng, Dr. Sathya Guruswamy, and Katherine Kudla for their guidance throughout this project, and my fellow REU students for their consistent help.

[1] Z. Peng , C. L. Martin, Z. Chen, D. B. Fielding, X. Xu, T. Heckman, L. Ramambason, Y. Li , C. Carr, W. Hu, and et al., The Astrophysical Journal **981**, 171 (2025).
[2] R. Weaver, R. McCray, J. Castor, P. Shapiro, and R. Moore, The Astrophysical Journal **218**, 377 (1977).
[3] C. L. Martin, Z. Peng, and Y. Li, The Astrophysical Journal **966**, 190 (2024).
[4] S. Geen and A. de Koter, Monthly Notices of the Royal Astronomical Society **509**, 4498–4514 (2021).
[5] D. E. Osterbrock, *Astrophysics of gaseous nebulae and active galactic nuclei* (University Science Books, 1989).
[6] C. L. Martin, The Astrophysical Journal **465**, 680 (1996).
[7] J. P. Ostriker and C. F. McKee, Reviews of Modern Physics **60**, 1–68 (1988).
[8] M. Mingozzi, M. Garcia del Valle-Espinosa, B. L. James, R. J. Rickards Vaught, M. Hayes, R. O. Amorín, C. Leitherer, A. Aloisi, L. Hunt, D. Law, and et al., The Astrophysical Journal **985**, 253 (2025).

APPENDIX

Galaxy	Superbubble	k_ρ	t (Myr)	Radius (km)	ρ (g cm^{-3})	Ω (rad)	r_{50} (km)	V (km s^{-1})	L_w (erg s^{-1})
J0934	superbubble 1	0	7.90 ± 0.21	1.66e+16 ± 0.01e+16	1.64e-24 ± 0.27e-24	0.70 ± 0.26	2.54E+15 ± 6.21E+12	39.86 ± 1.12	2.79E+39 ± 4.73E+38
		1	7.90 ± 0.21	1.66e+16 ± 0.01e+16	1.64e-24 ± 0.27e-24	0.70 ± 0.26	2.54E+15 ± 6.21E+12	49.83 ± 1.4	2.13E+38 ± 3.61E+37
		2	7.90 ± 0.21	1.66e+16 ± 0.01e+16	1.64e-24 ± 0.27e-24	0.70 ± 0.26	2.54E+15 ± 6.21E+12	66.43 ± 1.86	1.49E+37 ± 2.51E+36
		2.75	7.90 ± 0.21	1.66e+16 ± 0.01e+16	1.64e-24 ± 0.27e-24	0.70 ± 0.26	2.54E+15 ± 6.21E+12	88.57 ± 2.8	2.82E+36 ± 4.82E+35
	superbubble 3	0	7.60 ± 0.23	1.00e+16 ± 0.01e+16	1.95e-24 ± 0.32e-24	1.35 ± 0.20	1.67E+15 ± 5.92E+12	25.06 ± 0.83	5.84E+38 ± 3.47E+37
		1	7.60 ± 0.23	1.00e+16 ± 0.01e+16	1.95e-24 ± 0.32e-24	1.35 ± 0.20	1.67E+15 ± 5.92E+12	31.32 ± 1.04	4.86E+37 ± 2.86E+36
		2	7.60 ± 0.23	1.00e+16 ± 0.01e+16	1.95e-24 ± 0.32e-24	1.35 ± 0.20	1.67E+15 ± 5.92E+12	41.76 ± 1.38	3.7E+36 ± 2.17E+35
		2.75	7.60 ± 0.23	1.00e+16 ± 0.01e+16	1.95e-24 ± 0.32e-24	1.35 ± 0.20	1.67E+15 ± 5.92E+12	55.68 ± 2.07	7.49E+35 ± 4.61E+34
	superbubble 6	0	7.90 ± 0.21	8.99e+15 ± 0.15e+15	2.50e-24 ± 0.41e-24	0.89 ± 0.16	2.54E+15 ± 6.21E+12	21.64 ± 0.68	2.58E+38 ± 1.83E+37
		1	7.90 ± 0.21	8.99e+15 ± 0.15e+15	2.50e-24 ± 0.41e-24	0.89 ± 0.16	2.54E+15 ± 6.21E+12	27.05 ± 0.84	3.63E+37 ± 2.54E+36
		2	7.90 ± 0.21	8.99e+15 ± 0.15e+15	2.50e-24 ± 0.41e-24	0.89 ± 0.16	2.54E+15 ± 6.21E+12	36.07 ± 1.13	4.67E+36 ± 3.26E+35
		2.75	7.90 ± 0.21	8.99e+15 ± 0.15e+15	2.50e-24 ± 0.41e-24	0.89 ± 0.16	2.54E+15 ± 6.21E+12	48.08 ± 1.69	1.4E+36 ± 1.01E+35
J0944	superbubble 1	0	2.45 ± 0.77	9.97e+15 ± 0.24e+15	8.22e-25 ± 49.90e-25	3.18 ± 0.67	3.36E+15 ± 1.61E+13	77.36 ± 24.39	1.03E+41 ± 9.97E+40
		1	2.45 ± 0.77	9.97e+15 ± 0.24e+15	8.22e-25 ± 49.90e-25	3.18 ± 0.67	3.36E+15 ± 1.61E+13	96.71 ± 30.49	1.73E+40 ± 1.67E+40
		2	2.45 ± 0.77	9.97e+15 ± 0.24e+15	8.22e-25 ± 49.90e-25	3.18 ± 0.67	3.36E+15 ± 1.61E+13	128.94 ± 40.65	2.65E+39 ± 2.57E+39
		2.75	2.45 ± 0.77	9.97e+15 ± 0.24e+15	8.22e-25 ± 49.90e-25	3.18 ± 0.67	3.36E+15 ± 1.61E+13	171.92 ± 55.57	9.08E+38 ± 9.2E+38
	superbubble 2	0	1.53 ± 0.12	3.85e+15 ± 0.24e+15	9.09e-25 ± 55.20e-25	0.81 ± 0.08	3.23E+15 ± 5.58E+13	47.83 ± 4.7	1.02E+39 ± 1.41E+38
		1	1.53 ± 0.12	3.85e+15 ± 0.24e+15	9.09e-25 ± 55.20e-25	0.81 ± 0.08	3.23E+15 ± 5.58E+13	59.79 ± 5.87	4.26E+38 ± 5.41E+37
		2	1.53 ± 0.12	3.85e+15 ± 0.24e+15	9.09e-25 ± 55.20e-25	0.81 ± 0.08	3.23E+15 ± 5.58E+13	79.72 ± 7.83	1.63E+38 ± 2.02E+37
		2.75	1.53 ± 0.12	3.85e+15 ± 0.24e+15	9.09e-25 ± 55.20e-25	0.81 ± 0.08	3.23E+15 ± 5.58E+13	106.29 ± 10.75	1.1E+38 ± 1.48E+37
J1016	superbubble 1	0	5.09 ± 0.19	4.67e+15 ± 0.20e+15	8.86e-24 ± 1.46e-24	0.33 ± 0.07	1.34E+15 ± 1.18E+13	17.45 ± 0.97	4.84E+37 ± 5.43E+36
		1	5.09 ± 0.19	4.67e+15 ± 0.20e+15	8.86e-24 ± 1.46e-24	0.33 ± 0.07	1.34E+15 ± 1.18E+13	21.81 ± 1.21	6.91E+36 ± 7.38E+35
		2	5.09 ± 0.19	4.67e+15 ± 0.20e+15	8.86e-24 ± 1.46e-24	0.33 ± 0.07	1.34E+15 ± 1.18E+13	29.08 ± 1.62	9.02E+35 ± 9.52E+34
		2.75	5.09 ± 0.19	4.67e+15 ± 0.20e+15	8.86e-24 ± 1.46e-24	0.33 ± 0.07	1.34E+15 ± 1.18E+13	38.77 ± 2.43	2.73E+35 ± 3.14E+34
J1418	superbubble 1	0	1.42 ± 0.08	8.71e+15 ± 0.43e+15	7.96e-24 ± 1.31e-24	0.73 ± 0.15	3.33E+15 ± 4.54E+13	116.6 ± 8.45	9.83E+40 ± 1.22E+40
		1	1.42 ± 0.08	8.71e+15 ± 0.43e+15	7.96e-24 ± 1.31e-24	0.73 ± 0.15	3.33E+15 ± 4.54E+13	145.75 ± 10.56	1.88E+40 ± 2.19E+39
		2	1.42 ± 0.08	8.71e+15 ± 0.43e+15	7.96e-24 ± 1.31e-24	0.73 ± 0.15	3.33E+15 ± 4.54E+13	194.34 ± 14.08	3.28E+39 ± 3.76E+38
		2.75	1.42 ± 0.08	8.71e+15 ± 0.43e+15	7.96e-24 ± 1.31e-24	0.73 ± 0.15	3.33E+15 ± 4.54E+13	259.12 ± 21.12	1.23E+39 ± 1.59E+38
J1044	superbubble 1	0	2.00 ± 0.50	8.80e+15 ± 0.22e+15	1.20e-24 ± 0.50e-24	0.67 ± 0.13	9.40E+14 ± 8.24E+11	83.67 ± 21.02	5.14E+39 ± 4.02E+39
		1	2.00 ± 0.50	8.80e+15 ± 0.22e+15	1.20e-24 ± 0.50e-24	0.67 ± 0.13	9.40E+14 ± 8.24E+11	104.58 ± 26.27	2.74E+38 ± 2.14E+38
		2	2.00 ± 0.50	8.80e+15 ± 0.22e+15	1.20e-24 ± 0.50e-24	0.67 ± 0.13	9.40E+14 ± 8.24E+11	139.45 ± 35.03	1.33E+37 ± 1.04E+37
		2.75	2.00 ± 0.50	8.80e+15 ± 0.22e+15	1.20e-24 ± 0.50e-24	0.67 ± 0.13	9.40E+14 ± 8.24E+11	185.9 ± 46.55	1.92E+36 ± 1.5E+36
	superbubble 2	0	2.00 ± 0.50	8.52e+15 ± 0.22e+15	1.20e-24 ± 0.50e-24	1.27 ± 0.15	1.31E+15 ± 1.15E+12	81 ± 20.36	8.29E+39 ± 6.29E+39
		1	2.00 ± 0.50	8.52e+15 ± 0.22e+15	1.20e-24 ± 0.50e-24	1.27 ± 0.15	1.31E+15 ± 1.15E+12	101.26 ± 25.45	6.36E+38 ± 4.81E+38
		2	2.00 ± 0.50	8.52e+15 ± 0.22e+15	1.20e-24 ± 0.50e-24	1.27 ± 0.15	1.31E+15 ± 1.15E+12	135.01 ± 33.93	4.46E+37 ± 3.37E+37
		2.75	2.00 ± 0.50	8.52e+15 ± 0.22e+15	1.20e-24 ± 0.50e-24	1.27 ± 0.15	1.31E+15 ± 1.15E+12	179.98 ± 45.89	8.47E+36 ± 6.55E+36

TABLE II: Derived quantities for each galaxy and superbubble. Entries are value ± error.

Notes. Uncertainties for J0944 were approximated due to the limited data available from the literature.

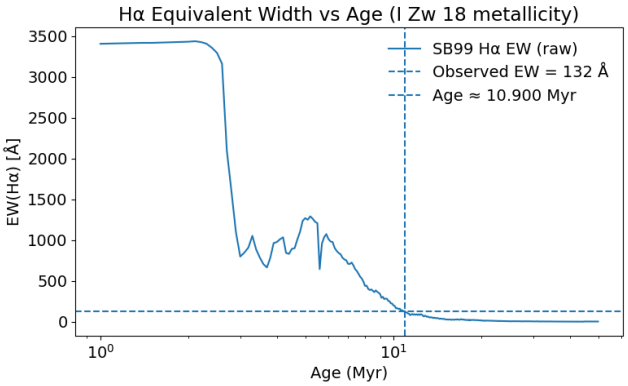

(a) Equivalent Width vs Age for the northwest star cluster (Cluster 1) in J0934

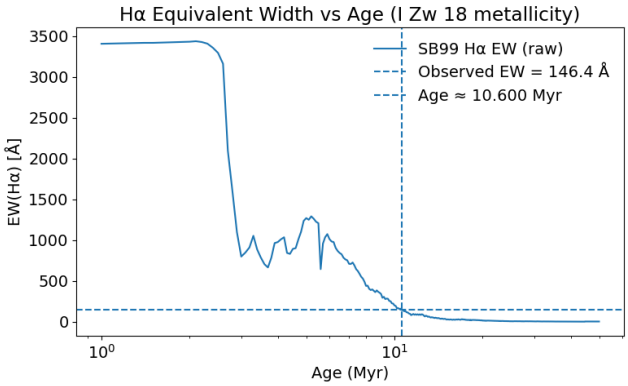

(b) Equivalent Width vs Age for the southeast star cluster (Cluster 2) in J0934

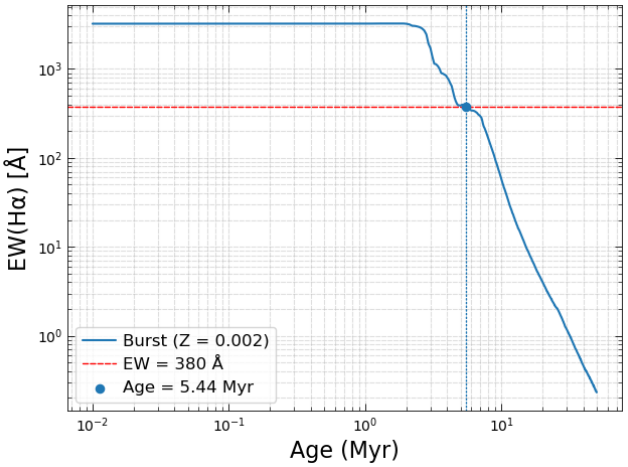

(c) Equivalent Width vs Age for the 3rd southern star cluster (Cluster 1) in J0944

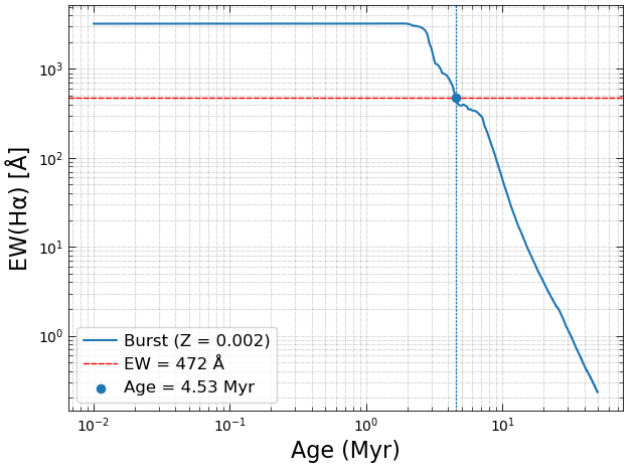

(d) Equivalent Width vs Age for the southernmost star cluster (Cluster 2) in J0944

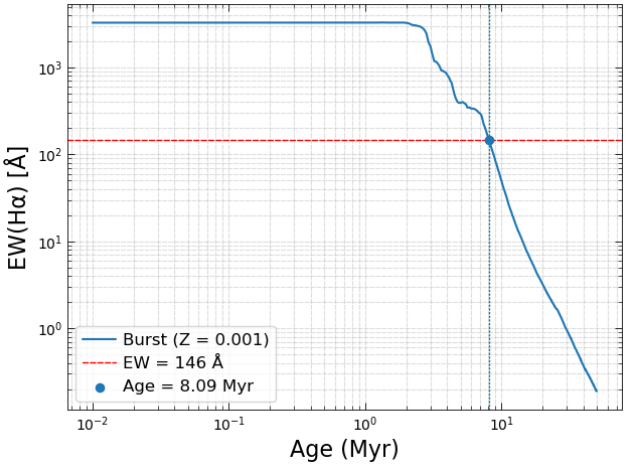

(e) Equivalent Width vs Age for the northernmost star cluster (Cluster 1) in J1016

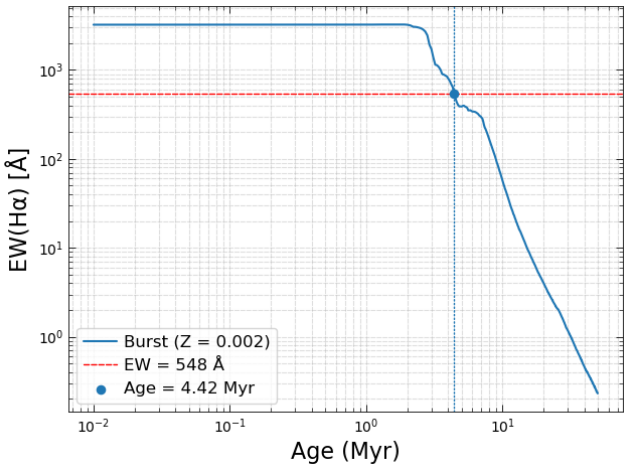

(f) Equivalent Width vs Age for the star cluster in J1418

FIG. 13

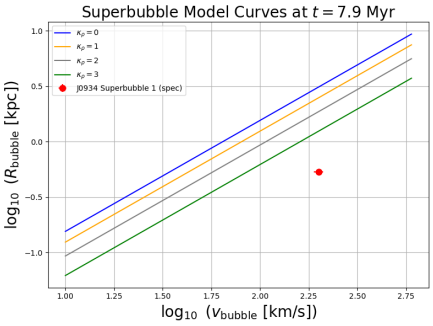

(a) Power Law Plot for superbubble 1 in J0934

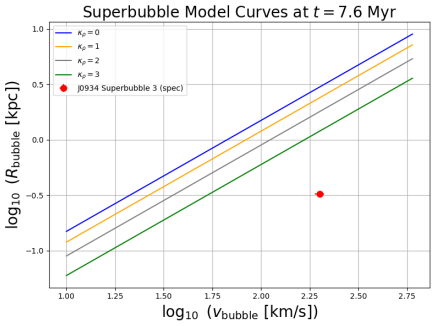

(b) Power Law Plot for superbubble 3 in J0934

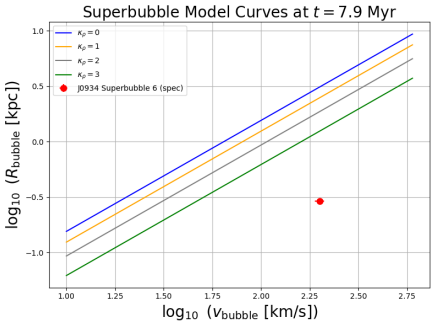

(c) Power Law Plot for superbubble 6 in J0934

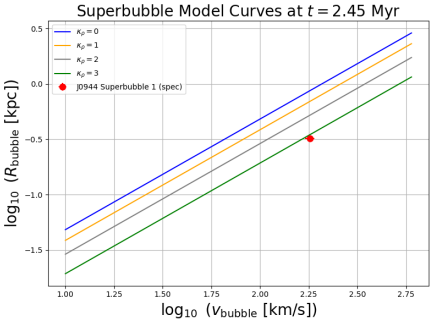

(d) Power Law Plot for superbubble 1 in J0944

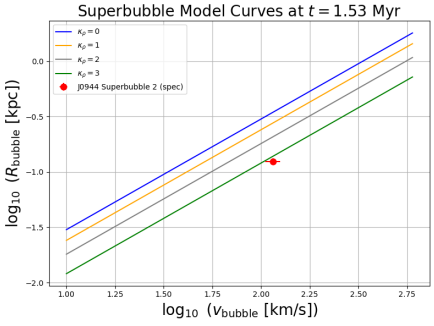

(e) Power Law Plot for superbubble 2 in J0944

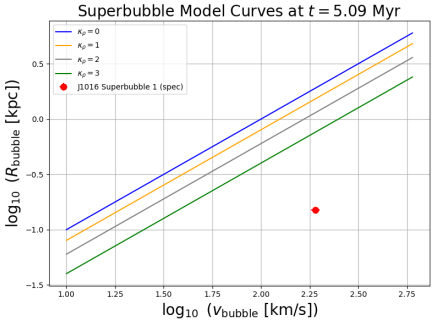

(f) Power Law Plot for the superbubble in J1016

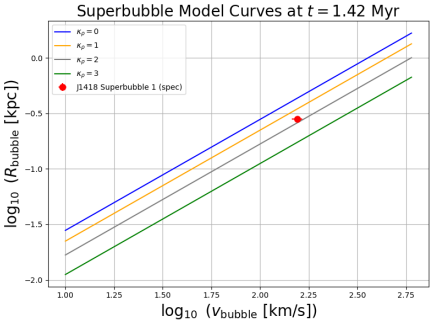

(g) Power Law Plot for the superbubble in J1418

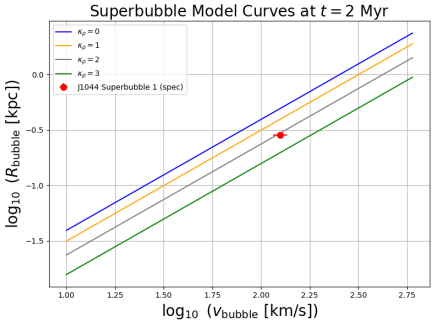

(h) Power Law Plot for superbubble 1 in J1044

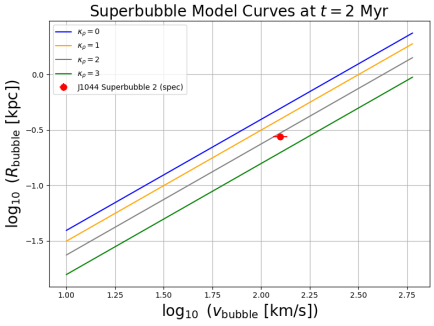

(i) Power Law Plot for superbubble 2 in J1044

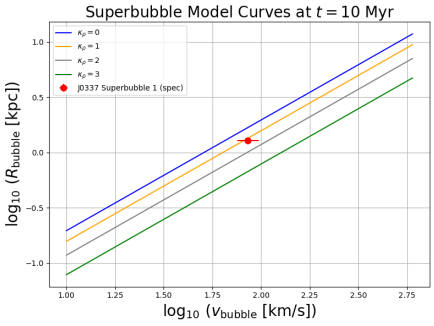

(j) Power Law Plot for the superbubble in J0337

FIG. 14

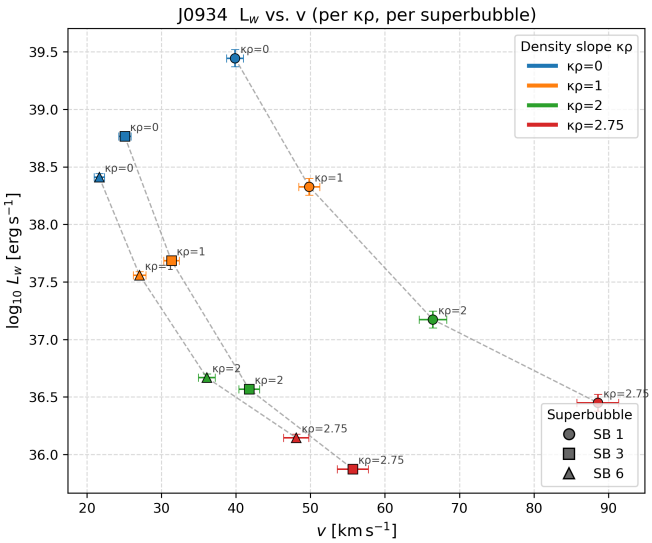

(a) Mechanical Luminosity vs Velocity for different density gradients for superbubbles in J0934

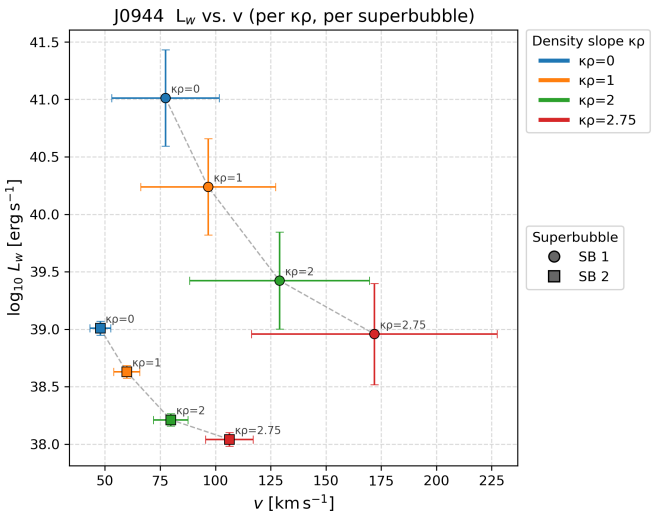

(b) Mechanical Luminosity vs Velocity for different density gradients for superbubbles in J0944

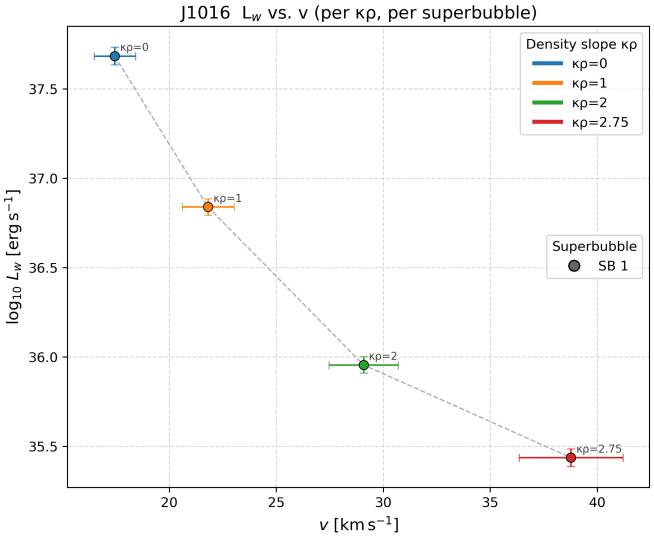

(c) Mechanical Luminosity vs Velocity for different density gradients for superbubble in J1016

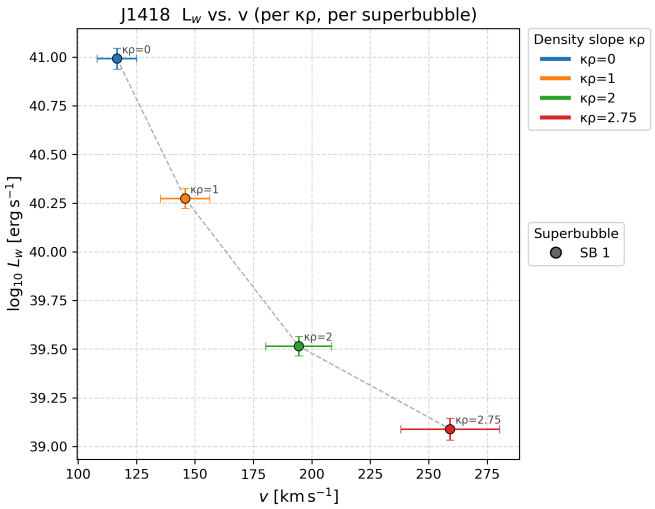

(d) Mechanical Luminosity vs Velocity for different density gradients for superbubble in J1418

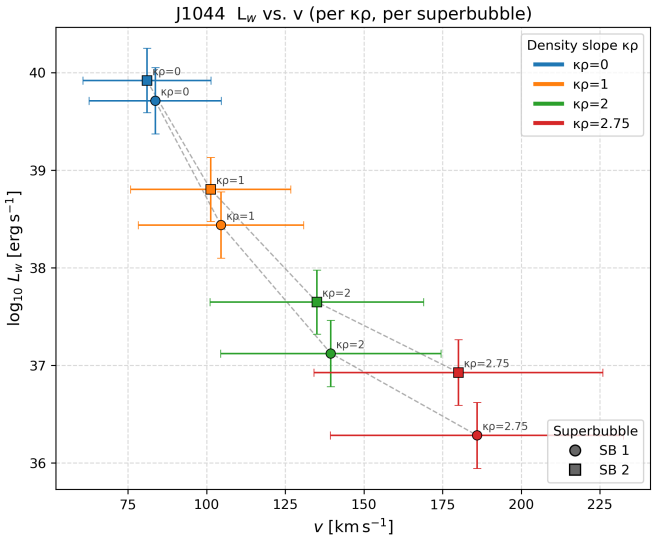

(e) Mechanical Luminosity vs Velocity for different density gradients for superbubbles in J1044

FIG. 15

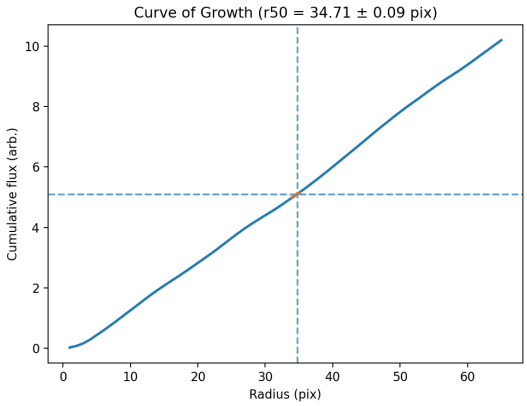

(a) J0934 NW cluster

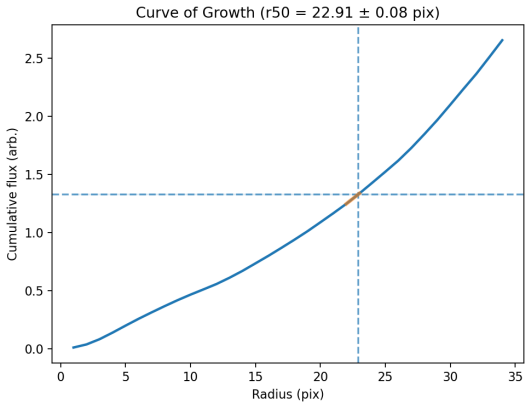

(b) J0934 SE cluster

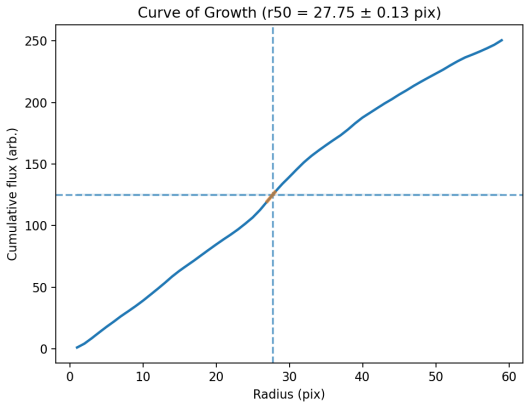

(c) J0944 North cluster

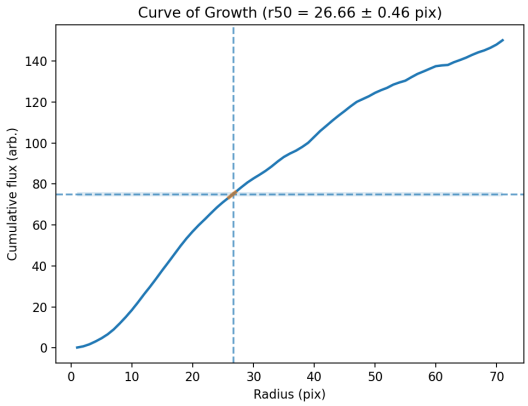

(d) J0944 South cluster

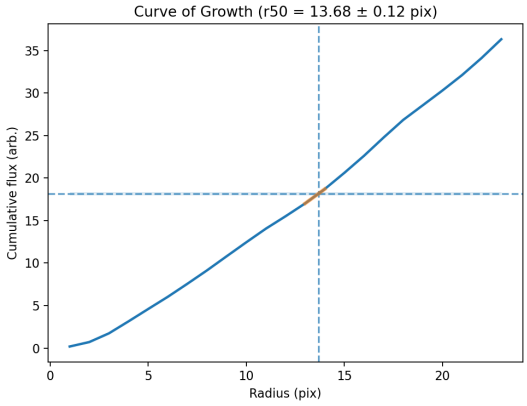

(e) J1016 cluster

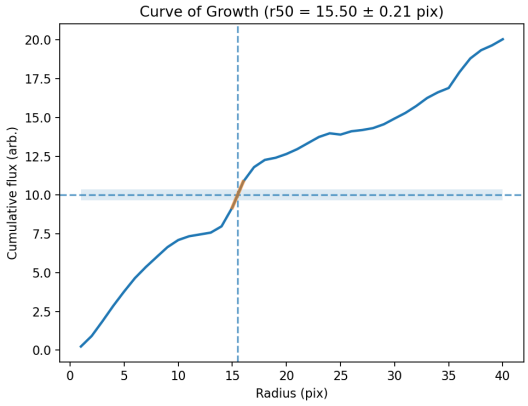

(f) J1418 cluster

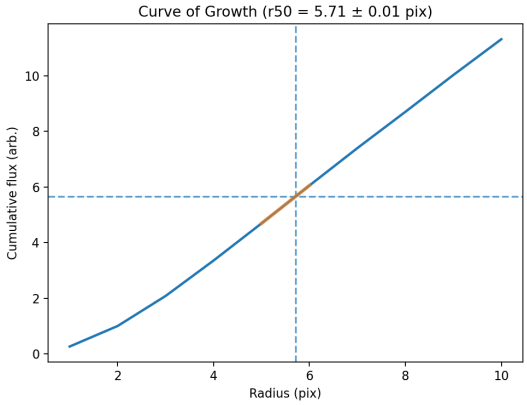

(g) J1044 North cluster

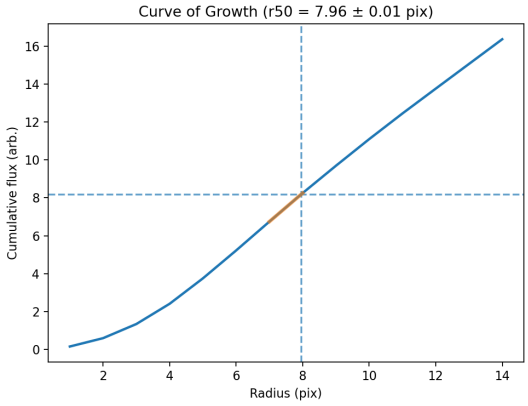

(h) J1044 South cluster

FIG. 16: Half-light radius (r_{50}) measurement plots for the star clusters powering the superbubbles. Each panel shows the curve of growth with r_{50} marked.